

# Production rates of long-lived radionuclides $^{10}\text{Be}$ and $^{26}\text{Al}$ under direct muon-induced spallation in granite quartz and its implications for past high-energy cosmic ray fluxes

H. Sakurai,<sup>1,\*</sup> Y. Kurebayashi,<sup>1</sup> S. Suzuki,<sup>1</sup> K. Horiuchi,<sup>2</sup> Y. Takahashi,<sup>1</sup> N. Doshita,<sup>1</sup> S. Kikuchi,<sup>1</sup> F. Tokanai,<sup>1</sup> N. Iwata,<sup>1</sup> Y. Tajima,<sup>1,3</sup> S. Gunji,<sup>1</sup> E. Inui,<sup>4</sup> K. Kondo,<sup>1</sup> T. Oe,<sup>1</sup> N. Sasaki,<sup>2</sup> S. Abe,<sup>5</sup> T. Sato,<sup>5</sup> H. Matsuzaki,<sup>6</sup> and V. Vlachoudis<sup>7</sup>

<sup>1</sup>Faculty of Science, Yamagata University, 1-4-12 Kojirakawa, Yamagata 990-8560, Japan

<sup>2</sup>Graduate School of Science and Technology, Hirosaki University,  
3, Bunkyo-chou, Hirosaki, Aomori 036-8561, Japan


<sup>3</sup>Institute of Arts and Sciences, Yamagata University, 1-4-12 Kojirakawa, Yamagata 990-8560, Japan

<sup>4</sup>Radio-isotopes Laboratory, Yamagata University, 1-4-12 Kojirakawa, Yamagata 990-8560, Japan

<sup>5</sup>Nuclear Science and Engineering Center, Japan Atomic Energy Agency,  
Tokai-mura, Naka-gun, Ibaraki 319-1195, Japan

<sup>6</sup>Micro-analysis Laboratory, Tandem Accelerator (MALT), The University Museum,  
The University of Tokyo, 2-11-16, Yayoi, Bunkyo-Ku, Tokyo 113-0032, Japan

<sup>7</sup>CERN, Geneva-23 CH-1211 Switzerland

 (Received 5 March 2023; revised 30 January 2024; accepted 29 February 2024; published 9 May 2024)

This study measured the  $^{10}\text{Be}$  and  $^{26}\text{Al}$  production cross sections of muon-induced long-lived radionuclides to investigate the long-term variations in high-energy cosmic ray muon yields and high-energy galactic cosmic rays over a few million years. We exposed targets consisting of synthetic silica plates and quartz samples in a 1-m-long granite core to a beam containing  $8.79 \times 10^{12}$  positive muons over  $\sim 120$  days with an energy of 160 GeV extracted at the COMPASS experiment line at CERN-SPS. The experiment revealed the  $^{10}\text{Be}$  and  $^{26}\text{Al}$  production rates in the synthetic silica plates as  $(1.8 \pm 0.1) \times 10^{-7}$  and  $(1.3 \pm 0.08) \times 10^{-6}$  atoms/muon/(g<sub>SiO2</sub>/cm<sup>2</sup>), respectively. In addition, we obtained the production rates in the granite core as approximately  $(4.1 \pm 0.2) \times 10^{-7}$  and  $(4.0 \pm 0.3) \times 10^{-6}$  atoms/muon/(g<sub>quartz</sub>/cm<sup>2</sup>) for  $^{10}\text{Be}$  and  $^{26}\text{Al}$ , respectively, although those rates varied with location. Furthermore, we performed full muon exposure simulations for the identical experimental setup using two simulators, PHITS and FLUKA, to examine the  $^{10}\text{Be}$  and  $^{26}\text{Al}$  production rates obtained in the muon beam experiment. The experimental rates are approximately 2–3 times higher than the simulated ones. Although the simulations are complex and depend on many models. Additionally, the PHITS and FLUKA analysis of the particle contributions to the  $^{10}\text{Be}$  and  $^{26}\text{Al}$  production rates indicated that the positive muons and secondary particles produce those nuclides at a constant rate and an increasing rate with respect to granite core location, respectively, suggesting direct muon-induced spallation and secondary particle-induced spallation. The experimental production ratio  $^{26}\text{Al}/^{10}\text{Be}$  also exhibited characteristics of both spallation types. We conclude that the production cross sections of  $^{10}\text{Be}$  and  $^{26}\text{Al}$  for the target atoms of oxygen and silicon were  $9.2 \pm 0.6 \mu\text{b}$  and  $132.3 \pm 7.7 \mu\text{b}$  via direct muon-induced spallation in the synthetic silica, and  $27.2 \pm 1.9 \mu\text{b}$  and  $486 \pm 44 \mu\text{b}$  including secondary particle-induced spallation in the granite quartz, respectively. Additionally, the depth profiles of  $^{10}\text{Be}$  and  $^{26}\text{Al}$  concentrations in rocks estimated from the known total muon flux deep underground and this study's cross sections were comparable to those of the concentrations measured at depths greater than 5000 g/cm<sup>2</sup>. Overall, our study showed that these cross sections revealed by the high-energy muon beam experiment are a valuable tool for estimating variations in high-energy galactic cosmic rays over a few million years using *in situ* rocks and simulators.

DOI: [10.1103/PhysRevD.109.102005](https://doi.org/10.1103/PhysRevD.109.102005)

## I. INTRODUCTION

Secular variations of galactic cosmic rays (GCRs) are associated with supernova explosions, cosmic ray confinement in supernova remnants, and cosmic ray propagation

\*Corresponding author: sakurai@sci.kj.yamagata-u.ac.jp

†Present address: Faculty of Science, Yamagata University, Yamagata 990-8560, Japan.

throughout the Galaxy. Although the average residence time of GCRs in the Galaxy is estimated as  $\sim 15$  million years (Myr) from the chemical composition of cosmic ray particles [1,2], it is still not known with certainty whether cosmic rays are well mixed in the Galaxy. The Solar System, which is moving at a speed around 10 km/s relative to near-by stars, rotates at a speed of 220 km/s with respect to the Galactic Center, passing through the galactic spiral arms [3]. So, the cosmic rays arriving at Earth presumably vary with the Solar System's location in the Galaxy on a timescale of a few million years. The recent observations of the enhanced  $^{60}\text{Fe}$  concentration in the deep ocean crust imply an event in which the Solar System passed through the vicinity of a supernova remnant  $\sim 2$  Myrs ago [4,5]. Still, research on the secular variations of GCRs requires careful consideration of galactic activities such as the formation and motion of spiral arms. Meanwhile, observations with the Tibet Air Shower arrays concerning the corotation relative to the local galactic magnetic field of GCRs with energies above a few hundred TeV [6] also show that it is very important to investigate past GCR fluxes above a few TeV. Because the Larmor radius for such high-energy GCRs is larger than the radius of the heliosphere, they are beyond the energy range affected by solar modulation and should consequently reflect the environments of the local galactic magnetic field, interstellar clouds, and nearby supernova remnants.

High-energy muons are produced in the atmosphere by high-energy GCRs and can penetrate deep underground, such as in Kamioka, where the average energy of a single muon is  $\sim 200$  GeV at a water-equivalent depth of 2 km [7]. Because deep underground rocks have been exposed to high-energy muons over a long time, the muon-induced radioisotopes  $^{10}\text{Be}$  and  $^{26}\text{Al}$  (with respective half-lives of  $1.36 \times 10^6$  yr and  $7.2 \times 10^5$  yr) have accumulated in these rocks. In rocks deeper than 100 m underground, these nuclides are primarily produced by muons with energies beyond 100 GeV, corresponding to GCRs of a few TeV [8]. Thus, the  $^{10}\text{Be}$  and  $^{26}\text{Al}$  concentrations in these deep underground rocks can be used to study the long-term variations in high-energy muon yields corresponding to those in high-energy GCRs over a few million years. Certain studies have analyzed  $^{10}\text{Be}$  and  $^{26}\text{Al}$  concentrations in rocks at depths shallower than 180 m for geoscience applications such as exposure dating and erosion rates [9–11]. However, drawing muon yields from those data requires further clarifying the mechanism of radioisotope generation by the muons in the rock. Muon-induced radionuclides are primarily produced by two processes: (1) direct muon-induced spallation of a nucleus via photonuclear interaction caused by virtual-photon exchange and (2) secondary particle-induced spallation, which consists of cascade reactions with the nuclei in a material with transmission of particles such as neutrons produced by other hadrons [7,12]. Therefore, cross sectional data of

radionuclide production are required for both direct muon and secondary-particle-induced spallation.

Only a single cross sectional dataset from radionuclide production in a 190 GeV muon beam experiment has been reported [13], wherein the targets for analyzing the produced radionuclide were placed behind a concrete block producing the muon-induced secondary particles. Balco used production models for cosmic ray muons to calculate cross sections from the measured depth profile of  $^{10}\text{Be}$  and  $^{26}\text{Al}$  concentrations in rock [11]. Therefore, this study conducted a muon exposure experiment to measure radionuclide production cross sections due to both direct muon-induced spallation and secondary particle-induced spallation without using any producer. A positive-muon beam with an energy of 160 GeV was used in COMPASS experiments [14] at the M2 beamline of CERN-SPS. The setup targets comprised synthetic pure-silica plates and a granite core (a rock sample) at the end of the COMPASS beamline, where they were exposed to the muon beam over  $\sim 120$  days. Then, we analyzed the radionuclides  $^{10}\text{Be}$  and  $^{26}\text{Al}$  produced in the target plates and the granite core using an accelerator mass spectrometry (AMS) system off-line.

The particle physics simulators FLUKA [15] and PHITS [16] use the photonuclear interaction cross-sections obtained from theoretical studies [17–19]. On the basis of the generalized vector dominance model, these cross sections have been evaluated from the virtual-photon exchange between a muon and a nucleus and/or nucleon. Hence, we have used both programs to simulate the radionuclides of  $^{10}\text{Be}$  and  $^{26}\text{Al}$  produced by direct muon-induced and secondary particle-induced spallation in a muon exposure experiment to check the validity of the experimental production rates.

This paper describes the production rates of the long-lived radioisotopes  $^{10}\text{Be}$  and  $^{26}\text{Al}$  in synthetic silica plates and the longitudinal profiles of the  $^{10}\text{Be}$  and  $^{26}\text{Al}$  production rates in quartz, which is a component of the granite core. In addition, the experimental production rates are compared with PHITS and FLUKA results. Finally, we present the  $^{10}\text{Be}$  and  $^{26}\text{Al}$  production cross sections caused by direct muon-induced and secondary particle-induced spallation for target oxygen and silicon atoms in synthetic silica and granite quartz, comparing with the published cross sectional data [11,13]. Furthermore, using this study's cross sections, we estimate the depth profiles of  $^{10}\text{Be}$  and  $^{26}\text{Al}$  concentrations in rocks from the known total muon flux deep underground and compare to those of the concentrations measured at depth.

## II. EXPERIMENT

### A. Targets and muon exposures

The primary target elements for  $^{10}\text{Be}$  and  $^{26}\text{Al}$  are oxygen and silicon, respectively. In the experiment, we used two kinds of muon exposure targets, which were manufactured

TABLE I. Chemical composition of the granite core samples (weight %) according to x-ray fluorescence analysis.

SiO <sub>2</sub>	TiO <sub>2</sub>	Al <sub>2</sub> O <sub>3</sub>	Fe <sub>2</sub> O <sub>3</sub>	MnO	MgO	CaO	Na <sub>2</sub> O	K <sub>2</sub> O	P <sub>2</sub> O <sub>5</sub>
75.7 ± 1.6	0.08 ± 0.06	13.0 ± 0.5	1.5 ± 0.7	0.06 ± 0.02	0.09 ± 0.1	1.0 ± 0.3	4.0 ± 0.2	5.1 ± 0.07	0.01 ± 0.015

synthetic silica plates (SiO<sub>2</sub>) [20] and a granite core containing approximately 30% quartz (SiO<sub>2</sub>). Silica plates were located in various positions including ones inserted between the granite core slices. Only those located in front of the granite core did not include muon-induced cascades because there was no other target material for cascades to start and develop. The synthetic silica plates were used to compare with the quartz in the granite core and to detect direct muon-induced spallation while reducing the associated secondary particle-induced spallation to the greatest possible extent. The impurities in the synthetic silica plates (with a density of 2.2 g/cm<sup>3</sup>) were less than 1 ppb for all substances except SiO<sub>2</sub>.

Granite quartz is mechanically tough enough to maintain its shape over several tens of millions of years, making it appropriate for detecting the secular variations of GCRs with timescales longer than the half-lives of <sup>10</sup>Be and <sup>26</sup>Al. Therefore, we usually choose granite quartz as the rock sample to detect the cosmic ray muon-induced nuclides <sup>10</sup>Be and <sup>26</sup>Al. The granite core used in this muon beam exposure experiment is a portion of a 1000-m-deep boring core sample obtained from the Toki granite rocks in

Japan [21]. The average density of the granite core is 2.57 g/cm<sup>3</sup>, and its chemical composition is listed in Table I with weight % as measured by x-ray fluorescence. The average quartz content of the granite core is 33% ± 3% by weight.

The experimental setup is illustrated in Fig. 1. The apparatus was placed at the end of the beam, close to the beam dump in the experimental hall and behind the COMPASS spectrometer. However, the space between the end detector of the COMPASS spectrometer and the experimental setup was ~5 m. No object was positioned between the spectrometer and the experimental apparatus. We measured the production rate resulting from direct irradiation of the target by a positive-muon beam with an energy of 160 GeV.

Figure 1 also shows that the apparatus contained a target box, a muon beam imager, a granite core, and plastic scintillation counters positioned in sequence along the muon beamline. Eight 5-mm-thick synthetic silica plates and three 2-mm-thick nickel plates were stacked in the target box with a 5-mm spacing. All plates were squares with a side length of 50 mm. Sandwiching the target plates,

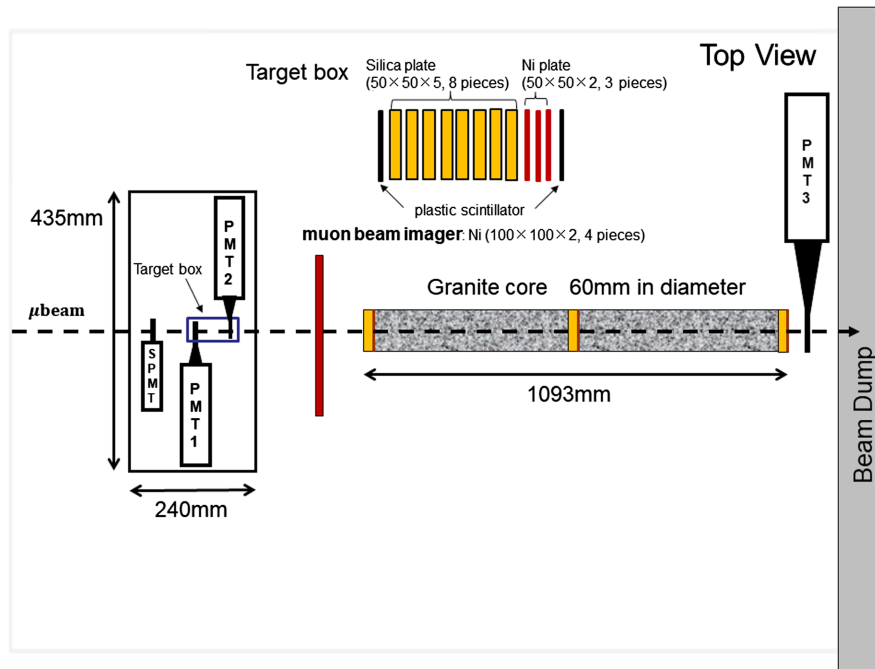


FIG. 1. Experimental setup at the beam stream’s tail on the COMPASS experiment line at CERN-SPS. The synthetic silica plates in the box and the 1-m-long granite core were on the beamline. The tiny black boxes attached to the tips of the PMTs are PLCs. All dimensions are in mm. The thicknesses of the silica plates and Ni plates are 5 and 2 mm, respectively.

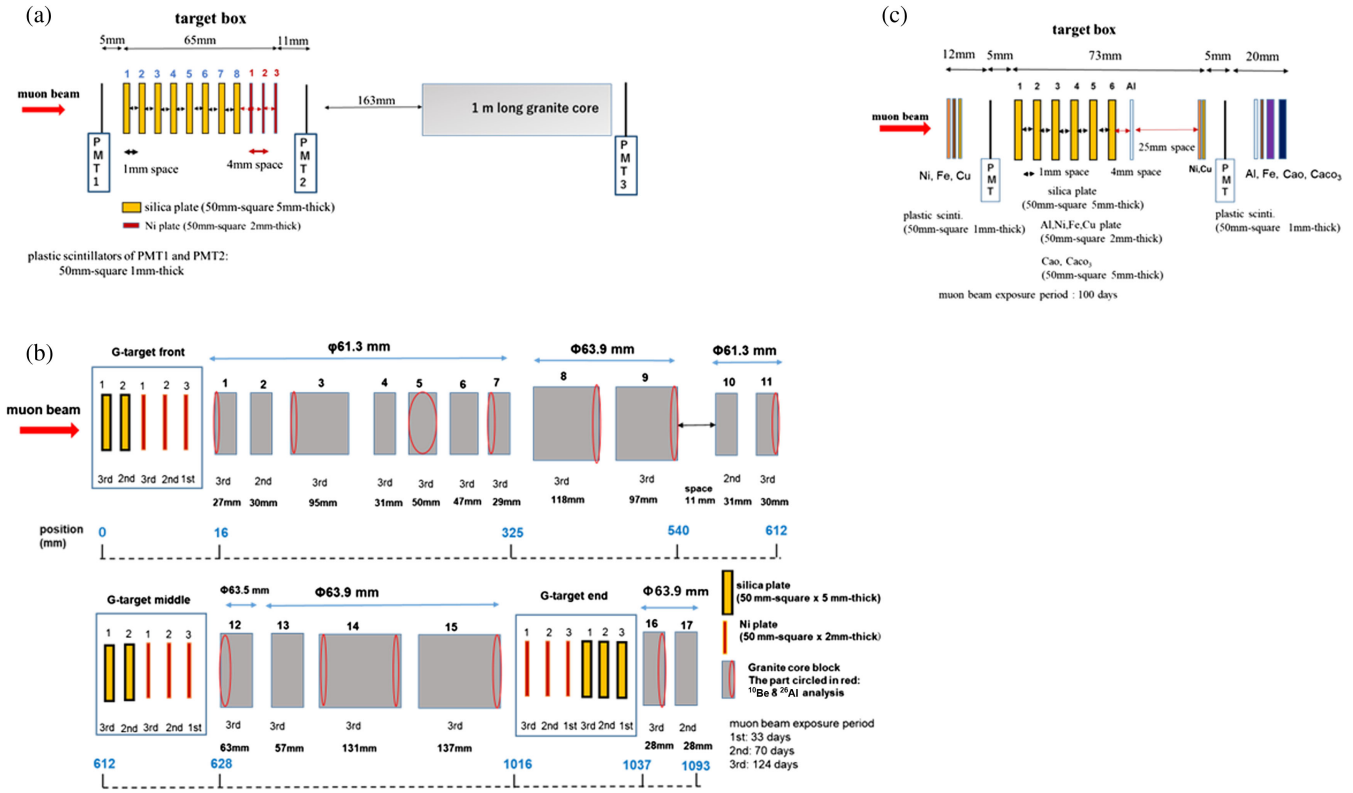


FIG. 2. Detailed setup (a) of the target box in Fig. 1. The silica plates and Ni plates are numbered 1 to 8 and 1 to 3. The muon exposure period of silica plates 1, 4, 5, and 8 was 124 days. For silica plates 2 and 7, the first muon exposure was for 70 days, and for silica plates 3 and 6, the first exposure was 33 days. Detailed setup (b) of the granite core in Fig. 1. The granite core blocks are numbered 1 to 17. G-target is a set of silica plates and Ni plates placed in front of and inserted between the granite core blocks. Another experimental setup (c) without a granite core sample installed at the beam stream’s tail on the COMPASS experiment line at CERN-SPS. See Table II.

we further mounted a 1-mm-thick, 50-mm-square plastic scintillator (PLC) at each end of the target box to count the incident muons. The granite core was  $\sim 1$  m long, comprising 17 divided pieces with a mounted a 5-mm-thick, 50-mm-square PLC at its end. Figure 2(a) shows the target sizes and positions in the target box as listed in Table II (target plate 1), and Fig. 2(b) shows the sizes and positions of the granite core samples according to Table II (granite core). Three sets of synthetic silica and nickel plates were placed at the front, in the middle, and at the end of the granite core samples to observe the effects of the muon-associated particles produced by the granite core on the plates, as shown in Fig. 2(b).

Subsequently, we monitored the two-dimensional muon beam profiles using nickel [22] and imaging plates to ensure that the targets were centered and exposed to uniform muon irradiation in the roughly elliptical beam (with vertical and horizontal dimensions of  $\sim 187$  and 124 mm, respectively). We irradiated the boxed silica plates and granite core samples with  $8.79 \times 10^{12}$  and  $(9.1\text{--}10.0) \times 10^{12}$  muons, respectively, for an exposure period of 124 d. Then, to examine the relationship between

the number of irradiating muons and the productions of  $^{10}\text{Be}$  and  $^{26}\text{Al}$ , we irradiated the silica plates in the target box during three different exposure periods, hence exposing the plates to different numbers of muons (Table III).

Specifically, as shown in Figs. 2(a) and 2(b), each silica plate and each granite core block was exposed to the muon beam for the first, second, and third periods. Therefore, in the first period all silica plates and granite core blocks were configured; we call this the first setup. In the second period, some silica plates assigned to the first in Fig. 2 were removed from the first setup while keeping all the granite blocks; we call this the second setup. Finally, in the third period, some silica plates assigned to the second and the three granite core blocks G2, G10, and G17 in Fig. 2 were removed from the second setup; we call this the third setup. Eventually, the number of irradiating muons for the first, second, and third setups are  $1.88 \times 10^{12}$ ,  $2.59 \times 10^{12}$ , and  $4.33 \times 10^{12}$  muons from Table III, respectively. The muon exposure experiments are further detailed in [23].

We also conducted another muon exposure experiment with solely a target box consisting of six synthetic silica

TABLE II. Sizes and numbers (target plate 1) of target plates in Figs. 2(a) and 2(b). Gtarget is a set of silica plates and nickel plates placed in front of and inserted between the granite core blocks in the middle and end sections. Sizes (granite core) of granite cores in Fig. 2(b). The locations of the front, middle, and back parts in Fig. 2(b) correspond to the granite core numbers. Sizes and numbers (target plate 2) of target plates in Fig. 2(c).

Target plate 1														
Plate	Target box				Gtarget front				Gtarget middle				Gtarget end	
	Silica		Nickel		Silica		Nickel		Silica		Nickel		Silica	Nickel
Square size (mm)	50		50		50		50		50		50		50	50
Thickness (mm)	5		2		5		2		5		2		2	5
Pieces	8		3		2		3		2		3		3	3

Granite core																	
Location	Front					Middle			Middle	Middle	Back			Back	Back	Back	
Core	G1	G2	G3	G4	G5	G6	G7	G8	G9	G10	G11	G12	G13	G14	G15	G16	G17
Diameter (mm)	61.3	61.3	61.3	61.3	61.3	61.3	61.3	63.9	63.9	61.3	61.3	63.5	63.9	63.9	63.9	63.9	63.9
Length (mm)	27	30	95	31	50	47	29	118	97	31	30	63	57	131	137	28	28

Target plate 2											
Plate	Front portion			Target box				End portion			
	Ni	Fe	Cu	Silica	Al	Ni	Cu	Al	Fe	CaO	CaCO <sub>3</sub>
Square size (mm)	50	50	50	50	50	50	50	50	50	50	50
Thickness (mm)	2	2	2	5	2	2	2	2	2	5	5
Pieces	1	1	1	6	1	1	1	1	1	1	1

plates, with no muon imager or granite core on the beamline, to investigate the effect of the granite core set on the target box. The targets were irradiated with  $1.55 \times 10^{13}$  muons lasting approximately 100 d. The detailed target setup is shown in Fig. 2(c) and Table II (target plate 2).

**B. Analysis of radionuclides in the targets**

The radionuclides <sup>10</sup>Be and <sup>26</sup>Al produced in the targets were analyzed using AMS at MALT, University of Tokyo [24,25]. First, the granite core target was sliced into several disks each with a thickness of ~5 mm, corresponding to various positions along the muon beamline as depicted in Fig. 2(b). Then, to obtain clean quartz grains from the disk samples, the standard procedure [26] was used to analyze the *in situ*-produced cosmogenic <sup>10</sup>Be and <sup>26</sup>Al. We crushed the silica plate samples in an iron mortar and washed the resulting fragments with 6 M HCl in an ultrasonic bath at

60°C for 3 h. Then, all the washed samples (both quartz grains and crushed silica plates) were dried and weighed. Subsequently, the samples were laced with 150 µg of <sup>9</sup>Be carrier and 300 µg of <sup>27</sup>Al carrier (the latter was used only for the silica plate samples), which were completely dissolved in a HF/HNO<sub>3</sub>/HClO<sub>4</sub> solution. Then, we performed ion exchange separation to isolate the Be and Al fractions, wherein the <sup>27</sup>Al concentrations in the samples were determined using graphite-furnace atomic-absorption spectrometry with a Hitachi Z-2710. These sample pretreatments and the atomic-absorption spectrometry analysis for the AMS preparation were conducted at Hirosaki University [27]. The <sup>10</sup>Be/<sup>9</sup>Be and <sup>26</sup>Al/<sup>27</sup>Al ratios measured with AMS were calibrated using the standard materials KNB5 – 2(8.56 × 10<sup>-12</sup>) and KNA5–1(4.69 × 10<sup>-12</sup>), respectively [28,29].

Subsequently, we measured the short-lived radionuclides <sup>7</sup>Be and <sup>22</sup>Na (with respective half-lives of 53.2 d and

TABLE III. Exposure periods and numbers of muons irradiated onto the silica plates in the target box.

Silica plate	No. 1	No. 2	No. 3	No. 4	No. 5	No. 6	No. 7	No. 8
Exposure period (days)	124	70	33	124	124	33	70	124
Irradiated muons (×10 <sup>12</sup> )	8.8	4.47	1.88	8.8	8.8	1.88	4.47	8.8

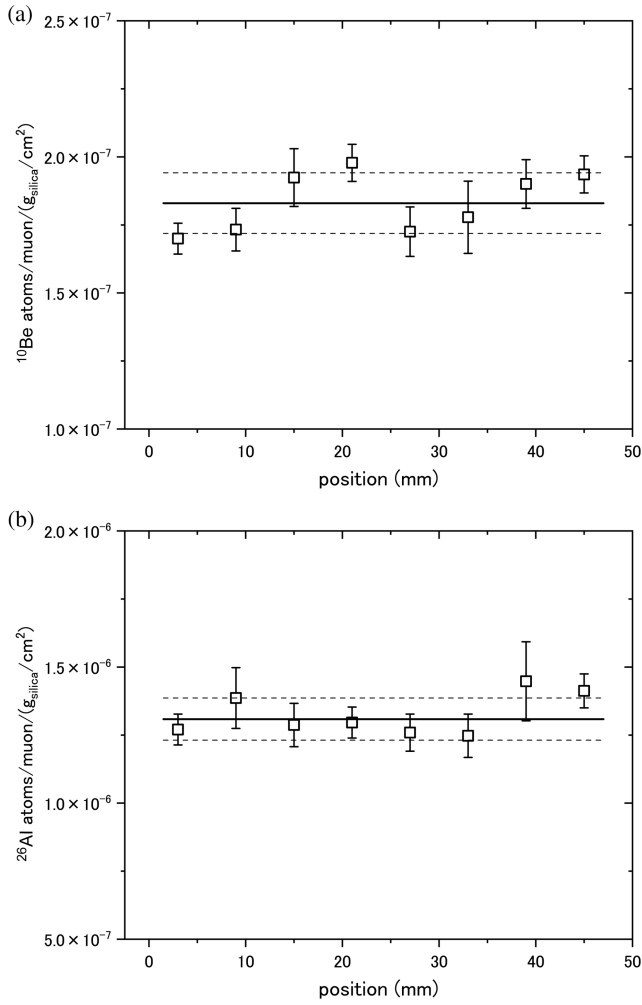


FIG. 3. Production rates of (a)  $^{10}\text{Be}$  and (b)  $^{26}\text{Al}$  in the eight synthetic silica plates of the target box. These rates were constant as indicated by the averages (black lines) and standard deviations (dashed lines).

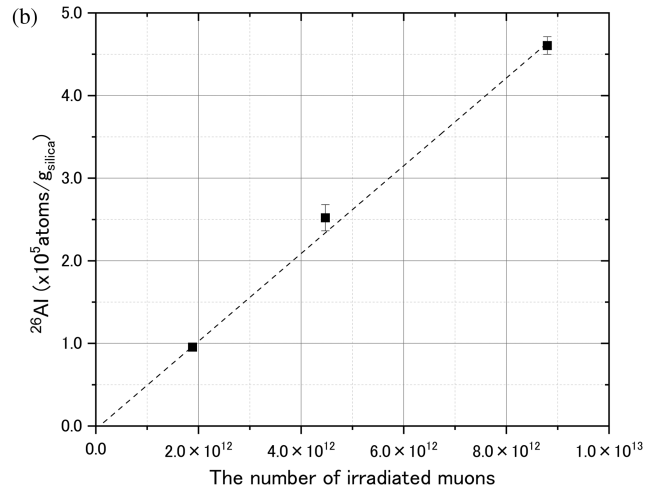
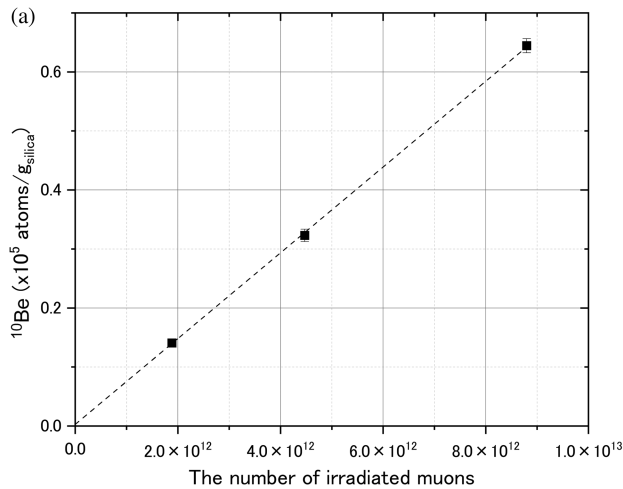


FIG. 4. Concentrations of (a)  $^{10}\text{Be}$  and (b)  $^{26}\text{Al}$  produced in the synthetic silica plates as functions of the number of irradiated muons. The values were well fitted by linear functions with negligible offsets.

2.6 yr) produced in the target silica plates to compare with the production profiles of the long-lived radionuclides  $^{10}\text{Be}$  and  $^{26}\text{Al}$ . Approximately one month after ceasing the muon exposure, we also measured the short-lived radionuclides off-line using a high-purity germanium gamma-ray detector shielded by an ultra-low-background lead (777B, Canberra), set up 20 m underground at the laboratory of the Institute for Cosmic Ray Research, University of Tokyo, without any destruction of the target plates.

### III. RESULTS AND DISCUSSION

#### A. Experimental results

##### 1. Production rates in the boxed silica plates

The production rates of the long-lived nuclides  $^{10}\text{Be}$  and  $^{26}\text{Al}$  detected in the silica plates stacked in the target box are depicted in Figs. 3(a) and 3(b), respectively. The average  $^{10}\text{Be}$  and  $^{26}\text{Al}$  production rates of the eight silica plates were  $(1.8 \pm 0.1) \times 10^{-7}$  and  $(1.3 \pm 0.08) \times 10^{-6}$  atoms/muon/ $(\text{g}_{\text{silica}}/\text{cm}^2)$ , respectively, with indicated standard deviations under 6%. This indicates that the production rates were almost constant. Furthermore, the  $^{10}\text{Be}$  and  $^{26}\text{Al}$  concentrations in the silica plates increased linearly with the number of irradiating muons with negligible offsets, as shown in Figs. 4(a) and 4(b) (Table III). This finding confirms the absence of any background contamination throughout the entire experiment.

Another muon exposure experiment was conducted with only the target box without granite core samples, as depicted in Fig. 2(c). The average  $^{10}\text{Be}$  and  $^{26}\text{Al}$  production rates measured in this experiment for the six silica plates were  $(1.8 \pm 0.05) \times 10^{-7}$  and  $(1.3 \pm 0.07) \times 10^{-6}$  atoms/muon/ $(\text{g}_{\text{silica}}/\text{cm}^2)$ , respectively, as shown in

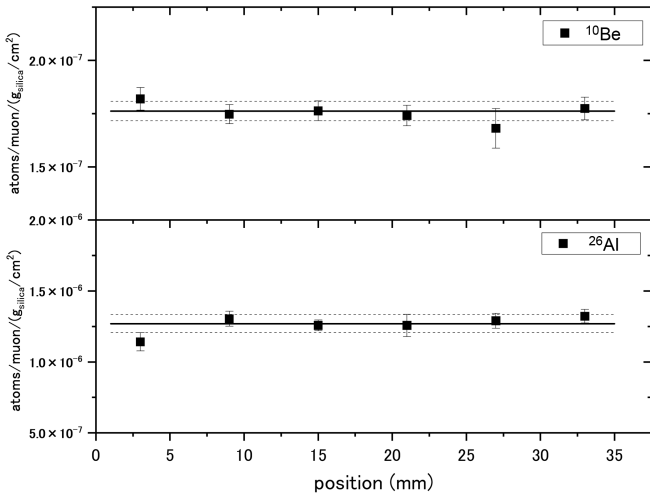


FIG. 5. Production rates of  $^{10}\text{Be}$  and  $^{26}\text{Al}$  in six synthetic silica plates during muon exposure experiments in the absence of a granite core. Both the average production rates (black lines) with standard deviations (dashed lines) were precisely the same as those in Figs. 3(a) and 3(b).

Figs. 5(a) and 5(b), which are basically the same rates as those of the previous muon exposure experiment. These results confirm that the nuclide productions with silica plates in the target box were unaffected by the granite core set behind the box, indicating the robustness of the data.

The average production rates of the short-lived nuclides  $^7\text{Be}$  and  $^{22}\text{Na}$  were  $(6.8 \pm 0.6) \times 10^{-7}$  and  $(6.1 \pm 1.1) \times 10^{-6}$  atoms/muon/(g<sub>silica</sub>/cm<sup>2</sup>), respectively, as shown in Fig. 6. These were approximately constant for each synthetic silica plate, as were the rates for the long-lived

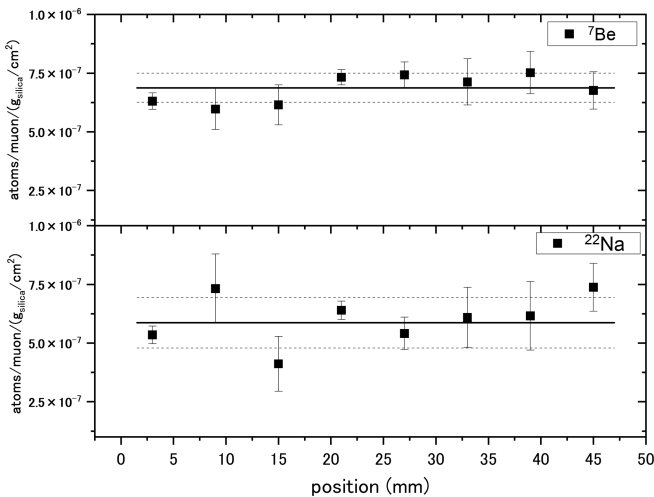


FIG. 6. Production rates of the short-lived nuclides  $^7\text{Be}$  and  $^{22}\text{Na}$  in the eight synthetic silica plates of the target box, respectively, including the averages (black lines) and standard deviations (dashed lines). They were constant, as were those of the long-lived nuclides  $^{10}\text{Be}$  and  $^{26}\text{Al}$  depicted in Fig. 3.

nuclides in the target box. This finding indirectly ensures the reliability of the long-lived production rate data because the rates displayed similarly constant profiles for each silica plate under various analysis methods.

Overall, the experimental results indicate consistent and constant production rates for all nuclides from each silica plate in the target boxes that are not significantly affected by other plates.

### 2. Production rates in the granite core

Muon beam irradiation of a granite core sample through silica plates in a target box implies a relationship between direct muon-induced spallation and secondary particle-induced spallation. Thus, data on the production rates of granite cores are significant and contributive in investigating the secular variation of cosmic rays from deep underground rocks. Figure 7 depicts the  $^{10}\text{Be}$  and  $^{26}\text{Al}$  concentrations under muon beam exposure of the 12 granite core samples as functions of position on the beamline with averages of  $(1.35 \pm 0.32) \times 10^5$  and  $(1.25 \pm 0.36) \times 10^6$  atoms/g<sub>quartz</sub>, respectively. The granite samples used in the muon beam experiment were recovered from depths of more than 300 m (see also Sec. II A). We investigated the contamination of *in situ*  $^{10}\text{Be}$  and  $^{26}\text{Al}$  concentrations using the granite sample not exposed to the muon beam and obtained from the G8 equivalent section of the original core (Table II). This was done by applying the same analytical procedure to the same amount of sample ( $\sim 10$  g quartz). The  $^{10}\text{Be}$  concentration was  $(4.1 \pm 3.7) \times 10^3$  atoms/g<sub>quartz</sub>, which is at the detection limit for  $\sim 10$  g of quartz and very low compared with the concentration of the muon beam-exposed sample from the same G8 section,

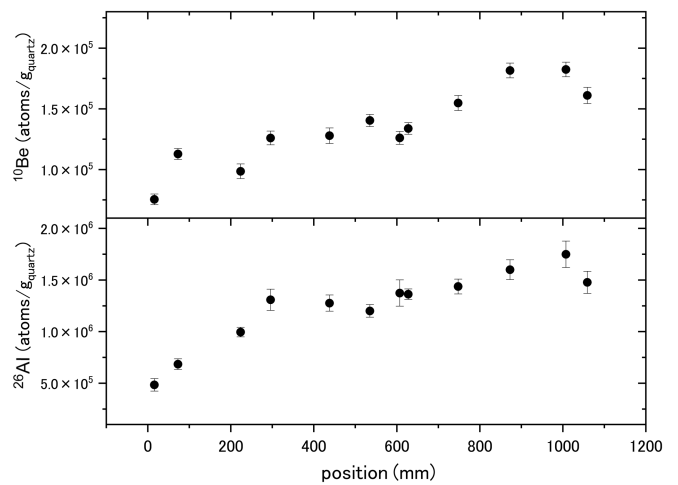


FIG. 7.  $^{10}\text{Be}$  and  $^{26}\text{Al}$  concentrations in the quartz samples extracted from the granite core as functions of the distance behind the front face of the core. The values indicate characteristic profiles of both nuclides.

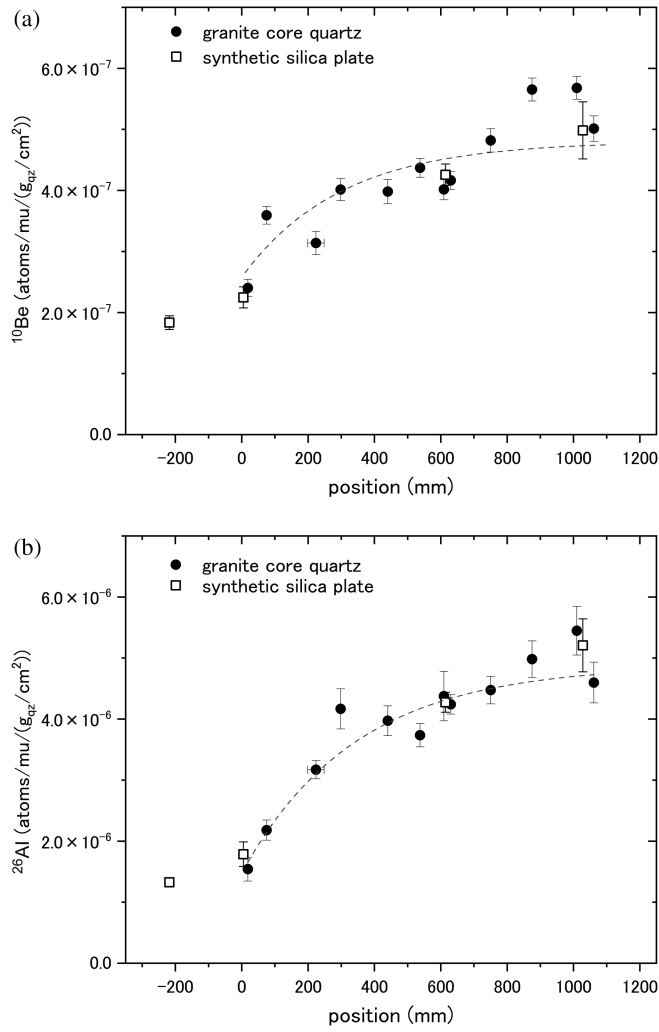


FIG. 8. Production rates of (a)  $^{10}\text{Be}$  and (b)  $^{26}\text{Al}$  in the granite core quartz as functions of the distance behind the front face of the granite core (black solid circles). Black open squares indicate the  $^{10}\text{Be}$  and  $^{26}\text{Al}$  production rates in the synthetic silica plates. The black open square on the left side of each figure indicates the average for the boxed synthetic silica plate targets. The dashed line is intended to guide the eye along the fitted exponential growth function.

$(1.28 \pm 0.07) \times 10^5$  atoms/g<sub>quartz</sub>. The  $^{26}\text{Al}$  concentration was below the detection limit.

Figures 8(a) and 8(b) shows the production rates of  $^{10}\text{Be}$  and  $^{26}\text{Al}$ , respectively, as functions of the sample position along the muon beam. The production rate is the normalized concentration relative to the total number of exposed muons monitored by the two PLCs of photomultipliers (PMT)1 and PMT3 in Fig. 1, taking account of the granite core area. The solid circles represent the production rates in the quartz extracted from the granite core samples, the open squares indicate the production rates in the synthetic silica plates placed at three positions along the granite core samples, and the open square on the left side of each figure

indicates the average for the boxed synthetic silica plate targets. The  $^{10}\text{Be}$  and  $^{26}\text{Al}$  production rates at the front of the granite core were similar to those of the boxed targets, which was consistent with the absence of significant material between the core and the targets. In contrast, the production rates in the granite core samples increased with the distance behind the front face of the granite core, as indicated by dashed lines in the figures.

In the middle portion approximately 500 mm and the back portion more than 700 mm into the granite core, the average production rates were  $(4.1 \pm 0.2) \times 10^{-7}$  and  $(5.5 \pm 0.4) \times 10^{-7}$  atoms/muon/(g<sub>quartz</sub>/cm<sup>2</sup>) for  $^{10}\text{Be}$  and  $(4.0 \pm 0.3) \times 10^{-6}$  and  $(4.9 \pm 0.4) \times 10^{-6}$  atoms/muon/(g<sub>quartz</sub>/cm<sup>2</sup>) for  $^{26}\text{Al}$ , respectively. Hence, the production rates in each portion are  $2.4 \pm 0.2$  and  $3.0 \pm 0.3$  times those of the boxed silica plates for  $^{10}\text{Be}$  and  $3.0 \pm 0.3$  and  $3.7 \pm 0.4$  times those of the boxed plates for  $^{26}\text{Al}$ , suggesting contributions of muon-induced secondary particles to the production rates. In addition, the  $^{10}\text{Be}$  and  $^{26}\text{Al}$  production rates in the back portion were  $32 \pm 15\%$  and  $21 \pm 15\%$  higher than those of the middle portion, respectively. These production rates were almost the same for the quartz samples extracted from the granite core and the inserted silica plates, confirming that the muon-induced secondary particles in the granite core irradiated the silica plates and their adjacent granite cores.

### 3. $^{26}\text{Al}/^{10}\text{Be}$ ratio

The depth profile of the  $^{26}\text{Al}/^{10}\text{Be}$  concentration ratio in a rock body is a useful indicator of high-energy cosmic ray muons over the past few hundred million years, owing to the long half-lives of these isotopes. However, distinguishing between cosmic ray and geological effects on rock samples requires interpreting the production rate ratio using the results of high-energy muon beam irradiation. Figure 9 depicts the  $^{26}\text{Al}/^{10}\text{Be}$  production ratios for the synthetic silica plates and the granite core quartz samples with black solid circles and black open squares, respectively, as functions of the granite core location. The average ratios for the silica plates directly irradiated by muons with an energy of 160 GeV were  $7.2 \pm 0.5$  and  $7.9 \pm 1.1$  in the target box and front of the granite core samples, respectively, implying direct muon-induced spallation. However, the ratios for the silica plates in the middle and back portions increased to  $10.1 \pm 0.6$  and  $10.5 \pm 1.3$ , respectively, under the influence of the secondary particles in the granite core. The ratios for the core quartz samples in the front and other portions of the granite were  $6.4 \pm 0.9$  and  $9.7 \pm 0.8$ , respectively. The increasing rates of the ratios from the front to the downstream portions in the granite core were comparable at  $1.5 \pm 0.3$  and  $1.3 \pm 0.2$ , respectively, for the granite core quartz and the synthetic silica plate.



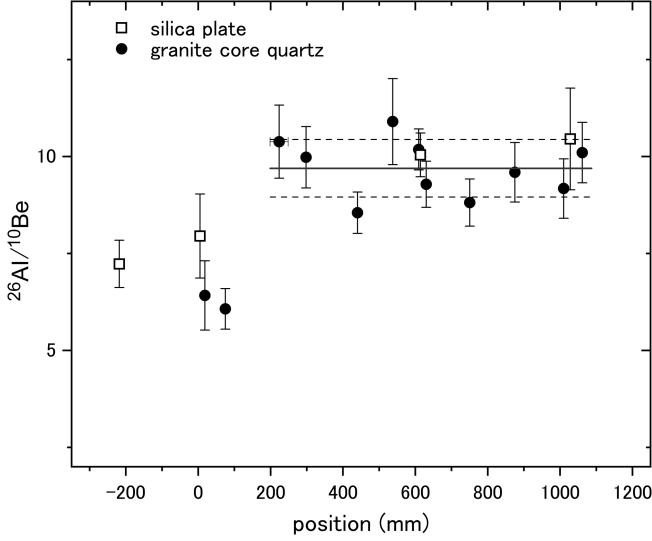


FIG. 9. Production rate ratios of  $^{26}\text{Al}$  and  $^{10}\text{Be}$  for the granite core quartz (black solid circles) and synthetic silica plates (black open squares). The position shows the distance behind the front face of the granite core. The black and dashed lines indicate the average and standard deviation for the granite core quartz data beyond 200 mm. The black open square on the left side indicates the average of the boxed synthetic silica plate targets.

To date, only two publications have reported data on such ratios in beam experiments:  $7.1 \pm 0.7$  in synthetic quartz irradiated with spallation neutrons produced from an 800 MeV proton beam [30] and  $7.5 \pm 0.1$  in a  $\text{SiO}_2$  disk (probably synthetic quartz) irradiated with a 190 GeV muon beam after transmission through a 3 m concrete block [13]. Both published data agree with our results for the synthetic silica plates. However, except for this study, no beam experimental data exist for the rock material,

although there is a report on a ratio attenuating from 6.8 to 3.4 in *in situ* rock quartz samples with depth [10,11].

## B. PHITS and FLUKA simulations

Finally, we performed full muon exposure simulations for the identical experimental setup in Figs. 2(a) and 2(b) and Table II using PHITS [16] and FLUKA [15]. The simulations were conducted to obtain  $^{10}\text{Be}$  and  $^{26}\text{Al}$  production rates in synthetic silica plates and in a granite core with the chemical composition in Table I, taking account of the muon exposure periods in Table III. Corresponding to the three muon exposure setups in the experiment described in the last part of Sec. II A, all three configurations were simulated, and the final production rates were obtained by weighting the production rates according to the number of irradiated muons in the experiment for each setup. The weighting factors of the first, second, and third setups were 1, 1.37, and 2.3, respectively.

The simulated  $^{10}\text{Be}$  and  $^{26}\text{Al}$  production rates are given in Table IV along with the experimental ones.

### 1. Simulated production rates in the boxed silica plates

Figures 10(a) and 10(b) shows the  $^{10}\text{Be}$  and  $^{26}\text{Al}$  production rates, respectively, of the silica plates in the target box as simulated by PHITS and FLUKA together with the experimental rates. The simulated and experimental production rates were clearly constant with respect to the silica plate location. However, the  $^{10}\text{Be}$  production rates in PHITS and FLUKA were only  $34 \pm 4\%$  and  $53 \pm 3\%$  as high as the experimental results, respectively. Furthermore, the  $^{26}\text{Al}$  production rates simulated in PHITS and FLUKA were only  $38 \pm 2\%$  and  $25 \pm 2\%$  as high as the experimental results, respectively.

TABLE IV. Simulated and experimental  $^{10}\text{Be}$  and  $^{26}\text{Al}$  production rates in the target box, each of the three portions of the granite core, and the whole granite core. Each value is given as the average and standard deviation.

	$^{10}\text{Be}$ ( $\times 10^{-7}$ atoms/mu/(g-qz/cm <sup>2</sup> ))							
	Target box	Front		Middle		Back		Whole
	Silica plate	Silica plate	Gcore	Silica plate	Gcore	Silica plate	Gcore	Gcore
Experiment	$1.8 \pm 0.1$	$2.3 \pm 0.2$	$2.4 \pm 0.2$	$4.3 \pm 0.2$	$4.1 \pm 0.2$	$5.0 \pm 0.5$	$5.5 \pm 0.4$	$4.2 \pm 1.0$
PHITS	$0.6 \pm 0.1$	$0.7 \pm 0.1$	$0.9 \pm 0.1$	$1.4 \pm 0.1$	$1.4 \pm 0.1$	$1.5 \pm 0.1$	$1.5 \pm 0.1$	$1.3 \pm 0.2$
FLUKA	$1.0 \pm 0.1$	$1.1 \pm 0.1$	$1.3 \pm 0.1$	$2.6 \pm 0.1$	$2.6 \pm 0.1$	$3.2 \pm 0.1$	$3.1 \pm 0.1$	$2.5 \pm 0.6$

	$^{26}\text{Al}$ ( $\times 10^{-6}$ atoms/mu/(g-qz/cm <sup>2</sup> ))							
	Target box	Front		Middle		Back		Whole
	Silica plate	Silica plate	Gcore	Silica plate	Gcore	Silica plate	Gcore	Gcore
Experiment	$1.3 \pm 0.1$	$1.8 \pm 0.2$	$1.5 \pm 0.2$	$4.3 \pm 0.2$	$4.0 \pm 0.3$	$5.2 \pm 0.4$	$4.9 \pm 0.4$	$3.9 \pm 1.1$
PHITS	$0.5 \pm 0.1$	$0.6 \pm 0.1$	$0.9 \pm 0.1$	$1.2 \pm 0.1$	$1.7 \pm 0.1$	$1.5 \pm 0.1$	$1.9 \pm 0.1$	$1.6 \pm 0.3$
FLUKA	$0.3 \pm 0.1$	$0.4 \pm 0.1$	$0.8 \pm 0.1$	$2.1 \pm 0.1$	$3.6 \pm 0.2$	$2.8 \pm 0.1$	$4.8 \pm 0.2$	$3.3 \pm 1.4$

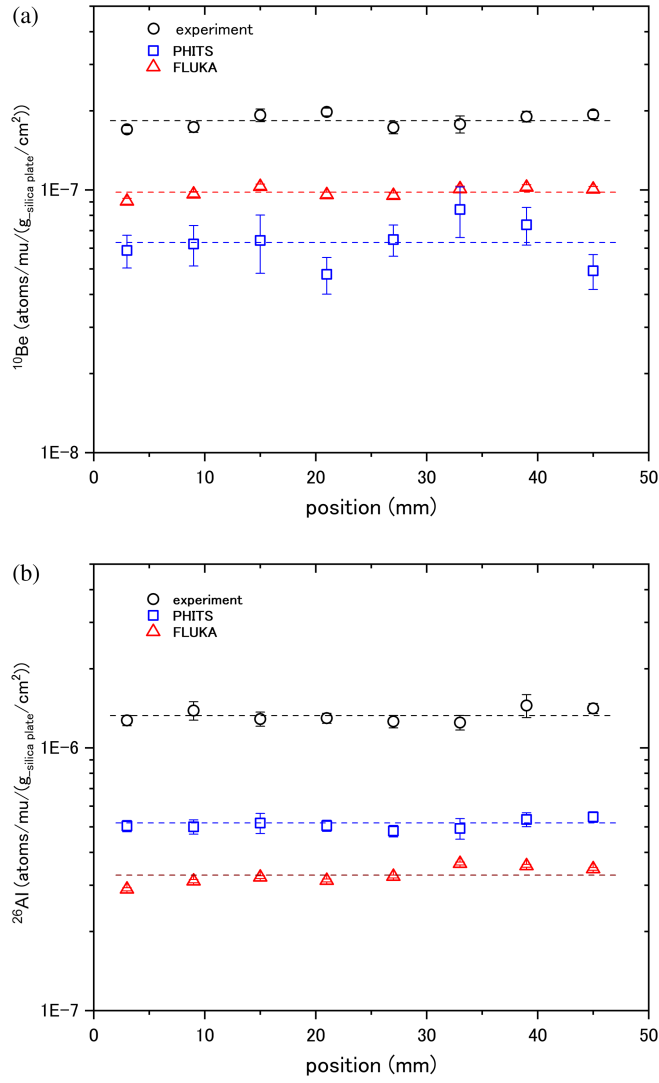


FIG. 10. Simulated (a)  $^{10}\text{Be}$  and (b)  $^{26}\text{Al}$  production rates of silica plates in the target box together with the experimental results (black open circles). The blue open squares and the red open triangles denote PHITS and FLUKA simulations, respectively. The dashed lines indicate their average values.

### 2. Simulated production rate in the granite core

Figure 11(a) shows the  $^{10}\text{Be}$  production rates of the silica plates and the quartz samples (Gcore) in the granite core simulated by PHITS and FLUKA together with the experimental results. As shown in Table IV, the simulated  $^{10}\text{Be}$  production rates of the silica plates in the granite core were comparable to those of the granite core quartz samples in both the PHITS and FLUKA simulations, like the experimental results. The simulated production rates rise steeply in the front portion of the granite core and then gradually increase further into the core, like the experimental results, as depicted in Fig. 11(a). As indicated for Gcore in Table IV, the  $^{10}\text{Be}$  production rates in the granite core simulated by PHITS and FLUKA were approximately

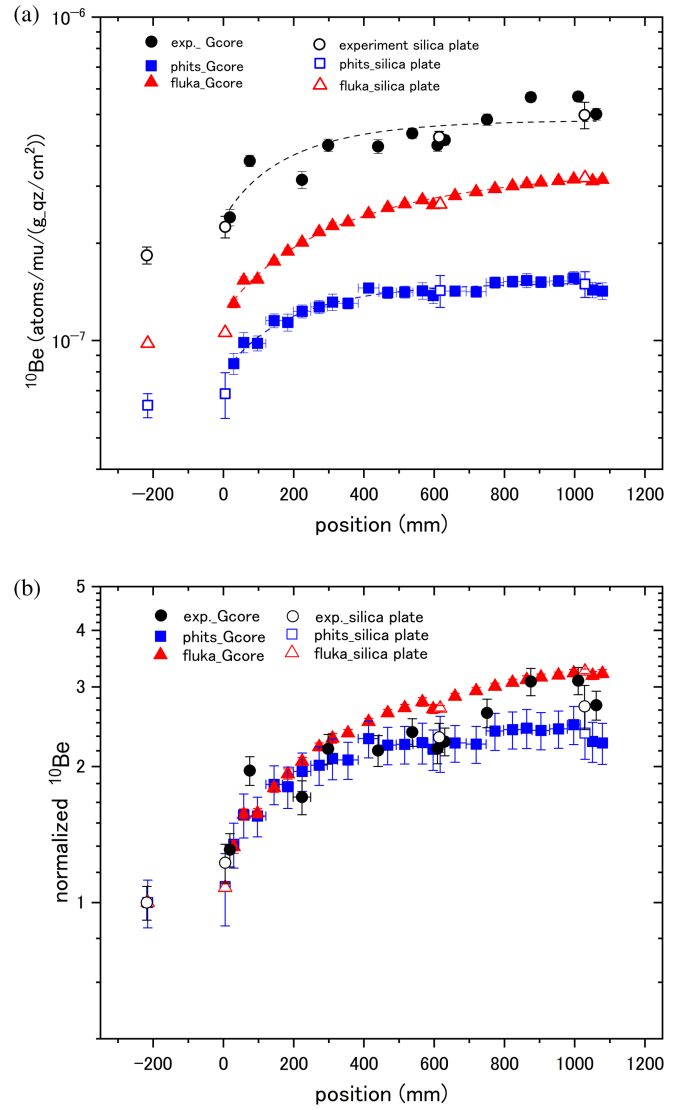


FIG. 11. (a) Simulated  $^{10}\text{Be}$  production rates of silica plates and quartz samples (Gcore) located in the granite core and (b) their values normalized to the average production rate of boxed silica plates, together with the experimental results (black solid circles). Blue solid squares and red solid triangles represent the PHITS and FLUKA simulations for the Gcore, respectively. Blue open squares and red open triangles represent the PHITS and FLUKA simulations for the silica plates, respectively, together with the experimental results (black open circles). Each dashed line in (a) is intended to guide the eye along a fitted exponential growth function. The position shows the distance behind the front face of the granite core.

$32 \pm 9\%$  and  $59 \pm 19\%$  as high as the experimental results on average, respectively. The ratios are similar to those of the silica plates in the target box described in the previous subsection. In Fig. 11(b), however, the  $^{10}\text{Be}$  production rates normalized to the rates for the boxed silica plates in the PHITS and FLUKA simulations are comparable to the normalized experimental results.

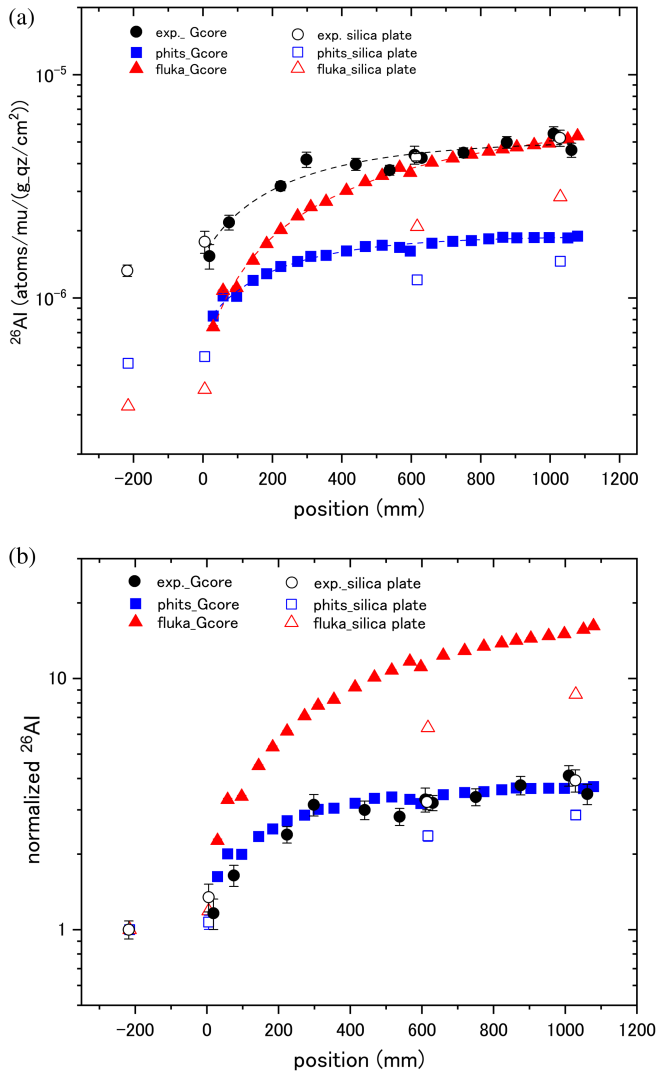


FIG. 12. (a) Simulated  $^{26}\text{Al}$  production rates of silica plates and quartz samples (Gcore) located in the granite core and (b) their values normalized to the average production rate of boxed silica plates, together with the experimental results (black solid circles). Blue solid squares and red solid triangles represent the PHITS and FLUKA simulations for the Gcore, respectively. Blue open squares and red open triangles represent the PHITS and FLUKA simulations for the silica plates, respectively, together with the experimental results (black open circles). Each dashed line in (a) is intended to guide the eye along a fitted exponential growth function. The position shows the distance behind the front face of the granite core.

Figure 12(a) shows the simulated  $^{26}\text{Al}$  production rates. Different from the  $^{10}\text{Be}$  rates in Fig. 11(a), the simulated  $^{26}\text{Al}$  production rates of the silica plates in the granite core were roughly  $75 \pm 3\%$  and  $59 \pm 5\%$  as high as those of the quartz samples in the PHITS and FLUKA simulations, respectively, while the experimental production rates of the quartz samples and the silica plates were comparable, as shown in Table IV. The PHITS and FLUKA production rates increase in a function similar to that of the  $^{10}\text{Be}$ . The  $^{26}\text{Al}$

production rates in the granite core simulated by PHITS and FLUKA were approximately  $40 \pm 14\%$  and  $85 \pm 45\%$  as high as the experimental results on average, respectively, as indicated for the whole Gcore in Table IV. The increase in the normalized  $^{26}\text{Al}$  production rates in PHITS was comparable to the normalized experimental results, as depicted in Fig. 12(b). However, the normalized  $^{26}\text{Al}$  production rates in FLUKA had a larger increase than that of the experimental results.

The experimental rates are 2–3 times higher than the calculated ones, and the difference is more than two standard deviations. We cannot conclude that the experimental data agree with the simulations. Taking into account that there is a difference between the simulations, the difference from experiment is because the simulations are complex and the models may not be accurate enough. There might be an inaccuracy in nuclear reaction models implemented in PHITS and FLUKA.

### 3. Simulated secondary particle-induced spallation in the granite core

The contribution of muon-induced secondary particles to the  $^{10}\text{Be}$  and  $^{26}\text{Al}$  production rates was simulated in the granite core and the silica plates using PHITS and FLUKA, and the difference in their  $^{26}\text{Al}$  production rates was investigated. Figure 13 shows the contribution of positive muons and muon-induced secondary particles, which are neutrons, photons, protons, pions, and negative muons, to the  $^{10}\text{Be}$  and  $^{26}\text{Al}$  production rates in the whole granite core and the whole silica plate. Figures 13(a) and 13(b) show that the particles contributing to the  $^{10}\text{Be}$  production rates are similar between both simulations, with positive muons ( $\sim 40\%$ ) being the main contributor, although the second contributor is photons in FLUKA. Additionally, the contribution of each particle to the  $^{10}\text{Be}$  production rates is similar between the granite core and the silica plate in both simulations. However, photons also significantly contribute to the  $^{26}\text{Al}$  production rate and are remarkable in FLUKA with a contribution of  $\sim 75\%$ , as shown in Figs. 13(c) and 13(d). Moreover, the contributions of photons to the  $^{26}\text{Al}$  production rates in the granite core are larger than those in the silica plate in both simulations.

Figures 14(a)–14(d) show the  $^{10}\text{Be}$  and  $^{26}\text{Al}$  production rates in the granite core and the silica plate via PHITS and FLUKA simulations. Each panel indicates profiles of positive muon-induced spallation with a constant rate and secondary particle-induced spallation due to neutrons and photons increasing with respect to granite core location.

In Figs. 14(a) and 14(b), the  $^{10}\text{Be}$  production rates due to the three particles in the silica plates placed in the granite core were similar to those of adjacent granite core in the middle ( $\sim 600$  mm) and back parts ( $\sim 1000$  mm). Additionally, in Figs. 14(c) and 14(d), the  $^{26}\text{Al}$  production rates in the silica plates due to positive muons and neutrons

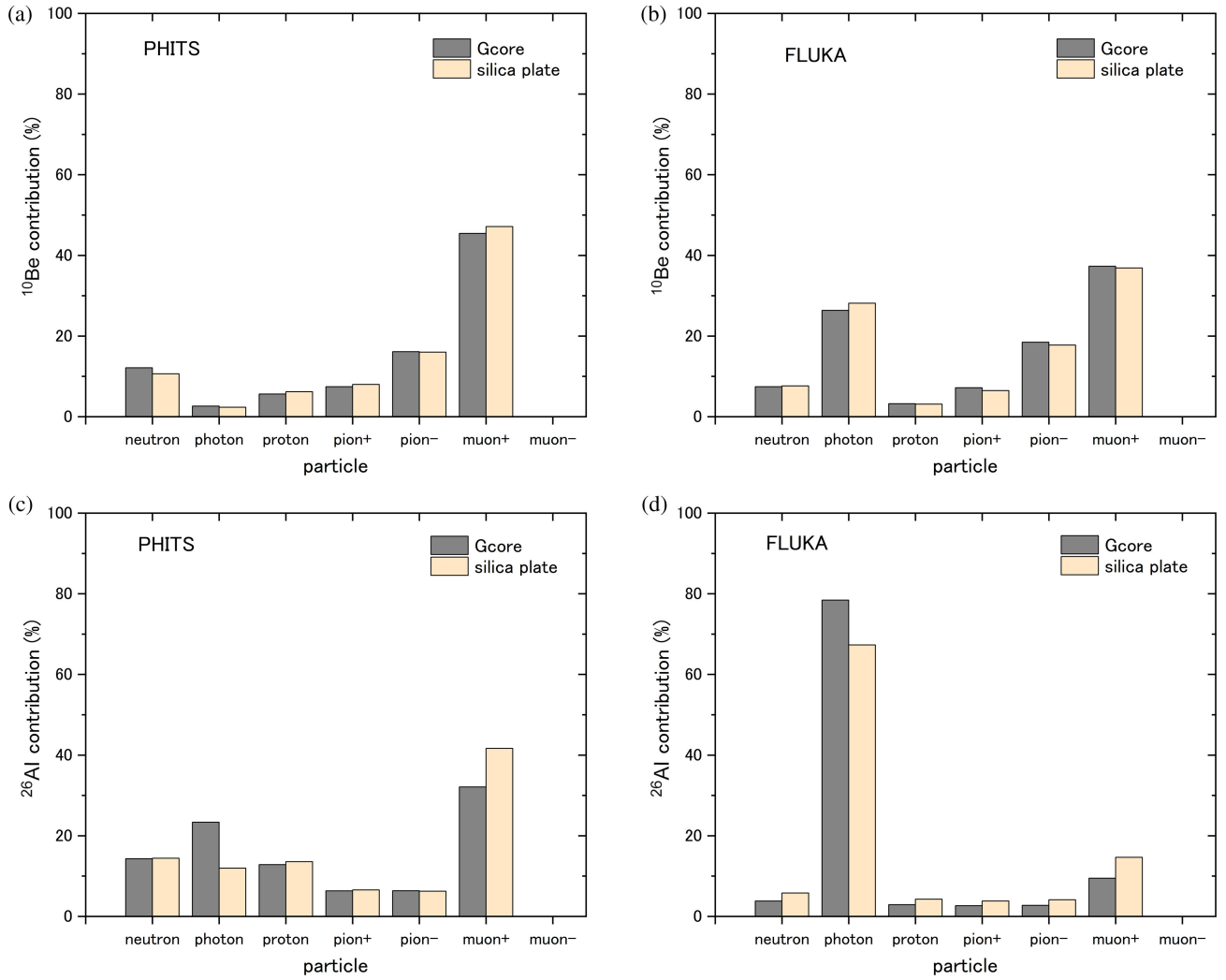


FIG. 13. Contributions of secondary particle-induced spallation to the  $^{10}\text{Be}$  [upper panels (a) and (b)] and  $^{26}\text{Al}$  [lower panels (c) and (d)] production rates in the whole granite core and the whole silica plate in PHITS and FLUKA simulations.

were similar to those of the granite core. However, according to PHITS in Fig. 14(c), the  $^{26}\text{Al}$  production rates of the silica plates due to photons were approximately 36% and 46% as high as those of granite core at the middle and back part, respectively. Similarly, according to FLUKA in the Fig. 14(d), the  $^{26}\text{Al}$  production rates of the silica plates due to photon were approximately 45% and 46% as high as those of the granite core in the middle and back part, respectively. In addition, taking account that the photon contribution to the simulated  $^{26}\text{Al}$  production rates is significant in the granite core, the simulations imply that the granite core matter shown in Table I is favorable for secondary production, especially photon production to produce the  $^{26}\text{Al}$ . Consequently, it is inferred that the simulated  $^{26}\text{Al}$  production rates in Fig. 12 mainly indicate the difference in  $^{26}\text{Al}$  production due to photons between the silica plate and the granite core.

Moreover, Fig. 15 compares the production rate ratios of  $^{26}\text{Al}$  to  $^{10}\text{Be}$  in the PHITS and FLUKA simulation with the experimental data, whose production rates in the silica plate are comparable with those in the granite core. The ratios increase in the granite core section compared with those in the front section as well as the experimental ratios, implying an effect of the secondary particle-induced spallation. However, the simulated ratios for the silica plates in the middle and back section are roughly constant and approximately within one standard deviation of the average experimental ratio for the granite core. Additionally, the simulated ratios for the granite core exceed two standard deviations of the average experimental ratio. These results suggest that the simulated  $^{26}\text{Al}$  production rates in the granite core may be overestimated relatively to the  $^{10}\text{Be}$  production rates.

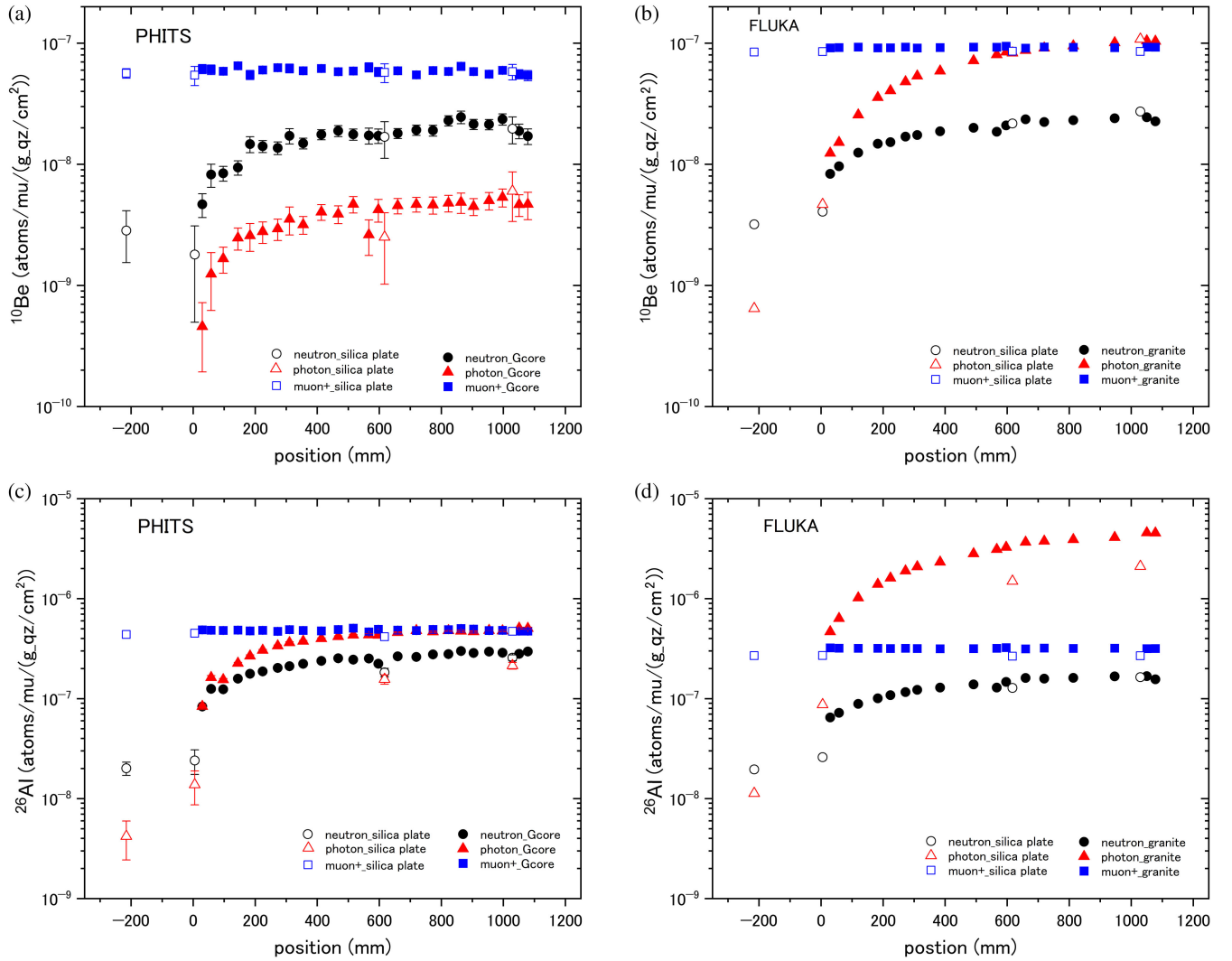


FIG. 14.  $^{10}\text{Be}$  and  $^{26}\text{Al}$  production rates in the granite core and the silica plate simulated via PHITS and FLUKA. Each panel indicates profiles of positive muon-induced spallation (blue solid and open squares) and secondary particle-induced spallation due to neutrons (black solid and open circles) and photons (red solid and open triangles). The  $^{26}\text{Al}$  production rates due to photons in the silica plates are evidently lower than those in the granite core in panels (c) and (d).

#### 4. Simulated production rates in different granite core setups

Figure 16 shows the  $^{10}\text{Be}$  and  $^{26}\text{Al}$  production rates simulated via PHITS and FLUKA for two muon exposure configurations of the first and second setup and the third setup. The first and second setup shows the weighted average production rates for the first and second setups keeping all the granite core blocks. As shown in the four panels of Fig. 16, the absence of the 31-mm-thick G10 granite core block in the third setup depicted in Fig. 2(b) affects the production rate of the 600-mm to 800-mm section, and there is no effect in the section behind 800 mm. The production rates in the middle section of the third setup are approximately 9% lower than those of the first and second setups. The PHITS values are  $8 \pm 3\%$  and  $10 \pm 7\%$  for the  $^{10}\text{Be}$  and  $^{26}\text{Al}$  production rates, respectively.

Additionally, the production rates in the back section are approximately 11% higher than those in the middle section in the third setup. Those PHITS values are  $12 \pm 4\%$  and  $11 \pm 9\%$  for the  $^{10}\text{Be}$  and  $^{26}\text{Al}$  production rates, respectively. These simulation profiles suggest that the increase in production rates at the back in Fig. 8 is related to the combination of three different configurations of granite core blocks in the experiment with muon beam irradiation conditions that are more complex than in the ideal simulation.

#### C. Cross sectional data

Table V compares the production cross sections of muon-induced long-lived radionuclides  $^{10}\text{Be}$  and  $^{26}\text{Al}$  for the target atoms of oxygen and silicon revealed by our 160 GeV muon exposure experiment with two reported

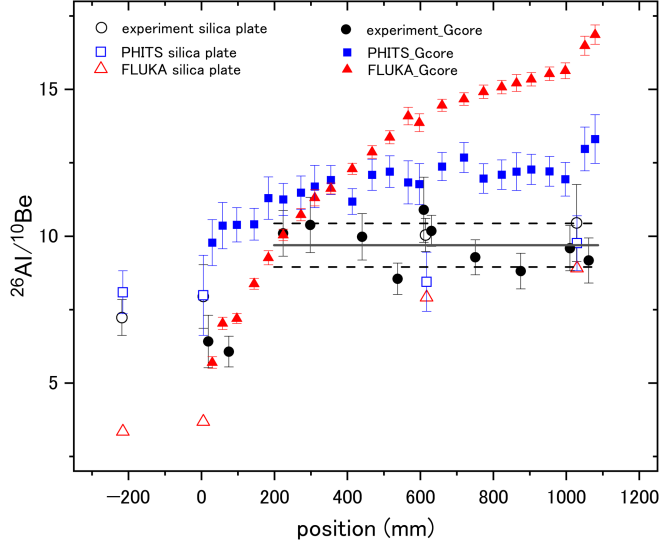


FIG. 15.  $^{26}\text{Al}$  to  $^{10}\text{Be}$  production rate ratios for the granite core (blue solid squares and red solid triangles) and the silica plate (blue open squares and red open triangles) simulated in PHITS and FLUKA, and corresponding experimental ratios in the granite core (black solid circles) and silica plate (black open circles). The black solid and dotted lines represent the average and standard deviation for the Gcore experiment. The position shows the distance behind the front face of the granite core.

cross section datasets. The cross sections were calculated from the experimental  $^{10}\text{Be}$  and  $^{26}\text{Al}$  production rates in Table IV as follows:

$$\sigma_{^{10}\text{Be}} = p_{^{10}\text{Be}} \cdot \frac{M_{\text{SiO}_2}}{2N_A} : \text{for oxygen atom}$$

$$\sigma_{^{26}\text{Al}} = p_{^{26}\text{Al}} \cdot \frac{M_{\text{SiO}_2}}{N_A} : \text{for silicon atom}$$

where  $\sigma$ ,  $p$ ,  $M$ , and  $N_A$  are the cross section, production rate, molecular weight, and Avogadro number, respectively.

The production cross sections of  $^{10}\text{Be}$  and  $^{26}\text{Al}$  were  $9.2 \pm 0.6 \mu\text{b}$  and  $132.3 \pm 7.7 \mu\text{b}$  for the target oxygen and silicon atoms in the boxed synthetic silica plates, respectively, indicating mainly direct muon-induced spallation. The production cross sections in the front granite core quartz were  $12.0 \pm 0.7 \mu\text{b}$  and  $154 \pm 20 \mu\text{b}$ , respectively, similar to those of the boxed silica plates. Furthermore, the  $^{10}\text{Be}$  and  $^{26}\text{Al}$  production cross sections in the granite core quartz were  $20.6 \pm 1.1$  and  $402 \pm 32 \mu\text{b}$  in the middle, respectively, and  $27.2 \pm 1.9$  and  $486 \pm 44 \mu\text{b}$  in the back portion, indicating the contribution of secondary particle-induced spallation.

Previously, Heisinger *et al.* reported single cross sections of  $94 \pm 13$  and  $1410 \pm 170 \mu\text{b}$  for  $^{10}\text{Be}$  and  $^{26}\text{Al}$  using a 190 GeV positive-muon exposure to a  $\text{SiO}_2$  target disk [13]. Even considering the effects of muon energy, the cross sections estimated for the 160 GeV muon were  $83 \pm 12$

$1240 \pm 150 \mu\text{b}$ , which are approximately 3.5 times larger than our results with the granite core. We infer that the target mounted behind a 3 m concrete block was exposed to a large amount of muon-induced secondary particles produced in the concrete block by the muon beam, and the contributions of the secondary particle-induced spallation appeared in the cross sections.

Balco calculated the cross sections from production models for cosmic ray muons using the measured  $^{10}\text{Be}$  and  $^{26}\text{Al}$  concentrations at different depths in rocks [11]. The cross sections for the 190 GeV muon were in the ranges 38–53  $\mu\text{b}$  for  $^{10}\text{Be}$  and 521–739  $\mu\text{b}$  for  $^{26}\text{Al}$ . However, at a muon energy of 160 GeV, they were in the ranges 33–47 and 458–650  $\mu\text{b}$  for  $^{10}\text{Be}$  and  $^{26}\text{Al}$ , respectively. These cross sections are consistent with our results obtained with the granite core in the muon beam exposure experiment.

### 1. Estimation of $^{10}\text{Be}$ and $^{26}\text{Al}$ concentrations in rocks

We estimated the depth profiles of  $^{10}\text{Be}$  and  $^{26}\text{Al}$  concentrations in rocks using the known total muon flux data at a depth underground [13] and the production cross sections. However, there might be further systematic uncertainties in the muon flux up to 20% due to the sample location and rock composition. Assuming nuclide radioactivity equilibrium, the  $^{10}\text{Be}$  and  $^{26}\text{Al}$  concentrations were calculated from the muon flux and the production cross sections at the average muon energy at each depth, respectively. At 5000 g/cm<sup>2</sup> underground (approximately 20 m deep), for instance, the muon flux is approximately  $2.1 \times 10^{-3}$  muons/cm<sup>2</sup>/s for an average muon energy of 20 GeV, which produces  $^{10}\text{Be}$  and  $^{26}\text{Al}$  in rock quartz at the rates of  $2.5 \times 10^{-10}$  and  $2.2 \times 10^{-9}$  atoms/g<sub>quartz</sub>/s, respectively.

Figures 17(a) and 17(b) shows the estimated  $^{10}\text{Be}$  and  $^{26}\text{Al}$  concentrations, respectively, in the rock quartz as functions of underground depth together with measured *in situ* rock concentrations up to 49300 g/cm<sup>2</sup> deep [10]. The black, blue, and orange dashed lines in the figure are for the cross sections of the middle and back quartz, and [13] in Table V, respectively, not including the cross sections of neutron spallation and muon capture. In the fast-muon region, the estimations from the cross sections obtained in our experiment were comparable to the measured concentrations at depths greater than 5000 g/cm<sup>2</sup>.

### 2. Possible age estimation of a cosmic ray anomaly

Because the formation of a rock body is generally a few tens of millions of years in the past, the  $^{10}\text{Be}$  and  $^{26}\text{Al}$  produced by cosmic ray muons accumulate in a rock deep underground over a long time, with continuous radioactive decay depending on their respective decay rates. Figure 18 shows a schematic linking the nuclide concentrations in rocks to the age estimation of a cosmic ray anomaly, if it

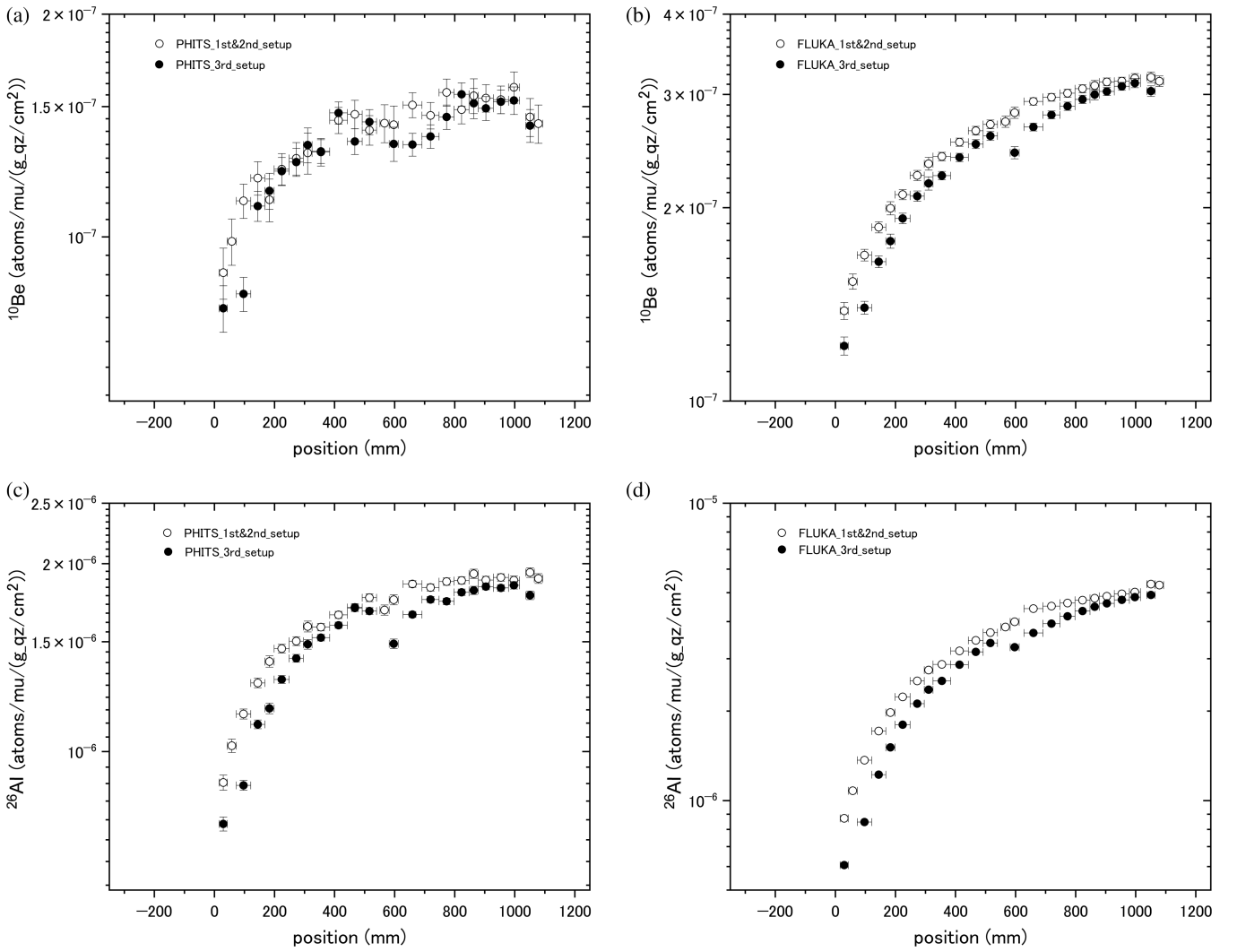


FIG. 16.  $^{10}\text{Be}$  and  $^{26}\text{Al}$  production rates simulated via PHITS and FLUKA for two muon exposure configurations of the granite core. The averaged production rates are shown for the first and second setups (black open circles) keeping all the granite core blocks. Three granite core blocks are absent in the third setup (black solid circles). See the main text for details about the configurations. The position shows the distance behind the front face of the granite core.

occurs. The diagram shows the case where cosmic ray muons increased to twice their current levels over a period of 1 Myrs starting 3 Myrs ago, as depicted in the bottom panel of the figure. Assuming that the steady-state muon flux is comparable to the current one, the steady-state concentrations of  $^{10}\text{Be}$  and  $^{26}\text{Al}$  in rocks are estimated using

the current muon flux and nuclide radioactivity equilibrium as indicated in Sec. III C 1. In the top panel, the concentrations of  $^{10}\text{Be}$  and  $^{26}\text{Al}$  in rocks are depicted as ratios to their steady-state concentrations and vary in response to the muon flux anomaly. The current  $^{10}\text{Be}$  and  $^{26}\text{Al}$  concentrations are 14.5% and 9% higher than the steady-state

TABLE V. Cross section data for  $^{10}\text{Be}$  and  $^{26}\text{Al}$  productions. The cross sections of the boxed silica plate and the three portions of granite core quartz were obtained in our muon exposure experiment. The uncertainties in this work are propagated from the errors in measured production rates in Table IV without any systematic error.

	Synthetic silica plate	Front quartz	Middle quartz	Back quartz	Heisinger <i>et al.</i> (190 GeV) [13]	Balco (190 GeV) [11]
$^{10}\text{Be}$ ( $\mu\text{b}$ )	$9.2 \pm 0.6$	$12.0 \pm 0.7$	$20.6 \pm 1.1$	$27.2 \pm 1.9$	$94 \pm 13$	$37.8 - 53.2$
$^{26}\text{Al}$ ( $\mu\text{b}$ )	$132 \pm 8$	$154 \pm 20$	$402 \pm 32$	$486 \pm 44$	$1410 \pm 170$	$521 - 739$

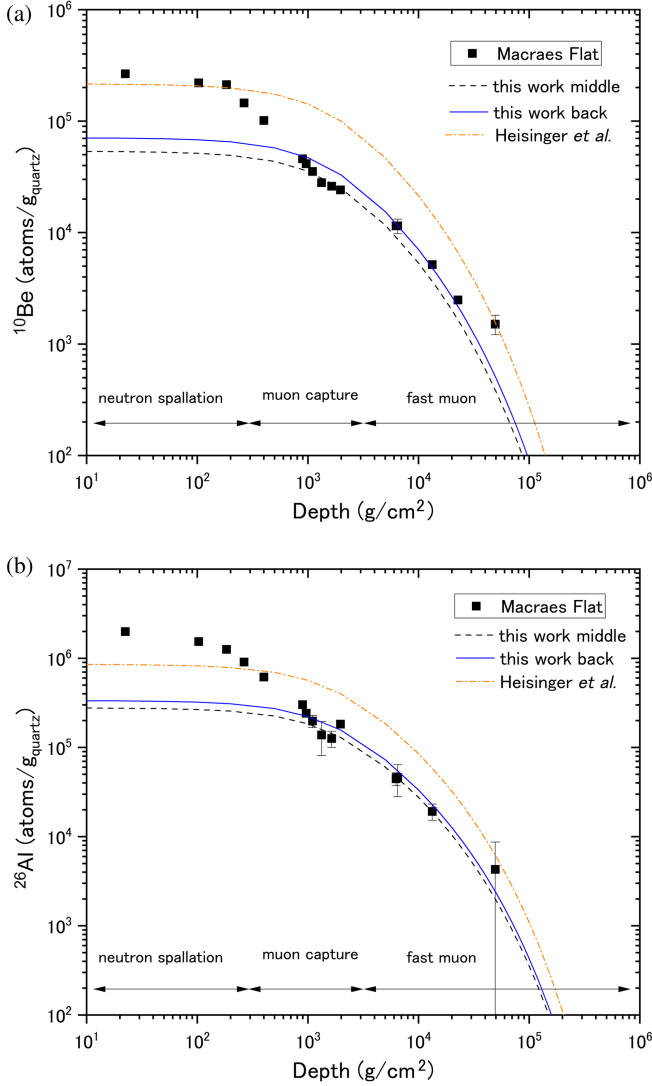


FIG. 17. Concentrations (black dashed line, blue line, and orange dashed-dotted line) of (a)  $^{10}\text{Be}$  and (b)  $^{26}\text{Al}$  in the rock quartz as functions of underground depth estimated from the muon flux and cross-section data. Black solid squares are measured *in situ* rock concentrations.

concentrations, respectively. Furthermore, the current  $^{26}\text{Al}/^{10}\text{Be}$  concentration ratio is 4.93 against the steady-state ratio of 5.15, as shown in the middle panel. In addition, in the case of a muon flux anomaly starting 2 Myrs ago (also for a period of 1 Myrs), the current  $^{10}\text{Be}$  and  $^{26}\text{Al}$  concentrations are 24.3% and 23.9% higher than the steady-state ones, respectively. We consider a case that the muon flux increases to approximately 20% compared with cosmic ray muons in the steady state. This is comparable to the uncertainty in the observed muon flux. In this case, the  $^{10}\text{Be}$  and  $^{26}\text{Al}$  concentrations become approximately 4.8% higher than the steady-state ones, which is a typical measurement error for those concentrations in rocks. Therefore, a cosmic ray anomaly 1.2 times

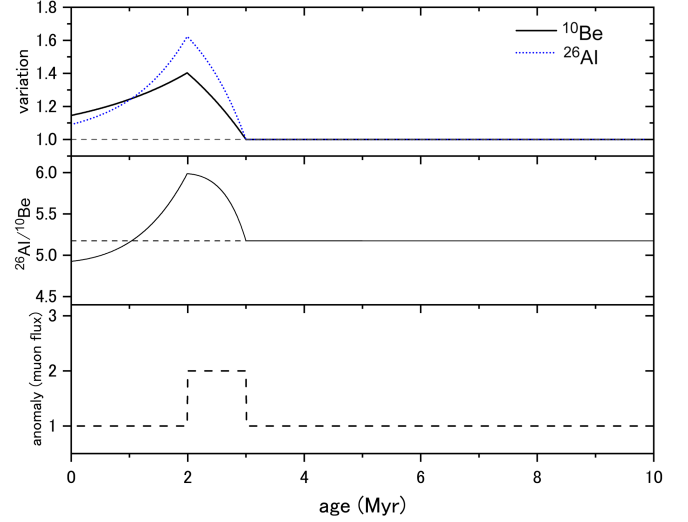


FIG. 18. Schematic linking the nuclide concentrations in rocks to the age estimation of a cosmic ray anomaly. The top and middle panels show responses of  $^{10}\text{Be}$  and  $^{26}\text{Al}$  concentrations and the ratio  $^{26}\text{Al}/^{10}\text{Be}$  in a rock to a cosmic ray anomaly depicted in the bottom panel (see the text).

as high as the steady-state flux would be a limitation of this method of age estimation. Thus, the age of a particular epoch can be investigated by comparing the measured  $^{10}\text{Be}$  and  $^{26}\text{Al}$  concentrations in rocks with the steady-state ones, although this depends on the event scale.

#### IV. CONCLUSIONS

We conducted a muon exposure experiment to measure the production cross sections of the muon-induced long-lived radionuclides  $^{10}\text{Be}$  and  $^{26}\text{Al}$  using a positive-muon beam with an energy of 160 GeV at the COMPASS experiment line at CERN-SPS. This study was essential for investigating long-term variations in high-energy cosmic ray muon yields and those in high-energy GCRs over a few million years, and for analyzing depth profiles of the  $^{10}\text{Be}$  and  $^{26}\text{Al}$  concentrations in deep underground rocks. Accordingly, a synthetic silica plate and a 1-m-long granite core target were set at the end of the line and exposed to a beam of  $8.79 \times 10^{12}$  muons over approximately 120 d. Then, we analyzed the  $^{10}\text{Be}$  and  $^{26}\text{Al}$  nuclides produced in the targets using AMS at MALT, University of Tokyo. Although the production rates in the boxed synthetic silica plates, which were located in front of the granite core target, were constant at  $(1.8 \pm 0.1) \times 10^{-7}$  and  $(1.3 \pm 0.08) \times 10^{-6}$  atoms/muon/(g $_{\text{SiO}_2}$ /cm $^2$ ) for  $^{10}\text{Be}$  and  $^{26}\text{Al}$ , respectively, the production rates in the granite core increased on the basis of location. Although the production rates for both  $^{10}\text{Be}$  and  $^{26}\text{Al}$  in the front portion of the granite core were comparable to those of the boxed silica plates, those in the back portion increased to  $3.0 \pm 0.3$  and  $3.7 \pm 0.4$  times as high as those of the boxed silica plates, respectively.



In addition, we performed full muon exposure simulations for the identical experimental setup using the two simulators PHITS and FLUKA to examine the  $^{10}\text{Be}$  and  $^{26}\text{Al}$  production rates obtained in the muon beam experiment. The simulated production rates in the boxed silica plates were clearly constant with respect to the silica plate location, as were the experimental rates. However, the  $^{10}\text{Be}$  production rates in PHITS and FLUKA were approximately 34% and 53% as high as the experimental ones, respectively. Similarly, the  $^{26}\text{Al}$  production rates in both simulations were approximately 38% and 25% as high as the experimental rates, respectively. Although the  $^{10}\text{Be}$  production rates in the granite core simulated by PHITS and FLUKA increased with target position similarly to the experimental ones, the average production rates were roughly 32% and 59% as high as the experiment values, respectively. Additionally, the  $^{26}\text{Al}$  production rates in PHITS and FLUKA showed an increase with target position similar to that of the experimental ones, although their averages were approximately 40% and 85% of the experimental values.

Furthermore, the PHITS and FLUKA analysis of the particle contribution to the  $^{10}\text{Be}$  and  $^{26}\text{Al}$  production rates indicated that positive muons produce those nuclides at a constant rate and secondary particles produce them at a rate that increases with respect to granite core location. This suggests direct muon-induced spallation and secondary particle-induced spallation. The analysis also indicated that the different  $^{26}\text{Al}$  production rates between the inserted silica plate and granite core is an effect of secondary photons in the simulations. In addition, the  $^{26}\text{Al}/^{10}\text{Be}$  production ratios of the inserted silica plates indicated a similar value to the experimental results, while the ratios for the granite core were larger than the experimental ones. The simulated  $^{26}\text{Al}$  production in the granite core is higher compared with the  $^{10}\text{Be}$  production. The simulations also

help reveal the relationship between the experimentally obtained production rate profiles and the granite core geometry in the muon exposure experiment.

Thus, we conclude that the experimental rates are approximately 2–3 times higher than the simulated ones. This is because the simulations are complex and depend on many models. This indicates that the total nuclear reaction cross sections of muons calculated by PHITS and FLUKA might be underestimated.

Finally, we conclude that the  $^{10}\text{Be}$  and  $^{26}\text{Al}$  production cross sections for the target atoms of oxygen and silicon were  $9.2 \pm 0.6 \mu\text{b}$  and  $132.3 \pm 7.7 \mu\text{b}$  via direct muon-induced spallation in the synthetic silica, and  $27.2 \pm 1.9 \mu\text{b}$  and  $486 \pm 44 \mu\text{b}$  including secondary particle-induced spallation in the granite quartz, respectively. This study's cross sections in the granite core were consistent with the results calculated from the measured depth dataset of the  $^{10}\text{Be}$  and  $^{26}\text{Al}$  rock concentrations [11]. Additionally, the depth profiles of  $^{10}\text{Be}$  and  $^{26}\text{Al}$  concentrations in rocks estimated from the known total muon flux deep underground and this study's cross sections were comparable to those of the measured concentrations at depths greater than  $5000 \text{ g/cm}^2$ .

## ACKNOWLEDGMENTS

The authors are greatly indebted to everyone on the COMPASS team who extensively supported this muon exposure experiment. The authors are also very grateful to the ICRR, which provided the low-background facility for measuring low-level radioactivity. Finally, we are deeply indebted to Dr. Kazuo Nakashima and Dr. Takashi Yuguchi for providing valuable data on the Toki granite samples. Part of this work was supported by JSPS KAKENHI (Grants No. JP15K05097, No. JP19H00706, and No. JP19K03882).

- 
- [1] M. Garcia-Munoz, G. M. Mason, and J. A. Simpson, *Astrophys. J.* **217**, 859 (1977).
  - [2] N. E. Yanasak, M. E. Wiedenbeck, R. A. Mewaldt, A. J. Davis, A. C. Cummings, J. S. George, R. A. Leske *et al.*, *Astrophys. J.* **563**, 768 (2001).
  - [3] F. J. Kerr and D. Lynden-Bell, *Mon. Not. R. Astron. Soc.* **221**, 1023 (1986).
  - [4] K. Knie, G. Korschinek, T. Faestermann, E. A. Dorfi, G. Rugel, and A. Wallner, *Phys. Rev. Lett.* **93**, 171103 (2004).
  - [5] A. Wallner, J. Feige, N. Kinoshita, M. Paul, L. K. Fifield, R. Golser, M. Honda *et al.*, *Nature (London)* **532**, 69 (2016).
  - [6] M. Amenomori, S. Ayabe, X. J. Bi, D. Chen, S. W. Cui, Danzengluobu, L. K. Ding *et al.*, *Science* **314**, 439 (2006).
  - [7] D.-M. Mei and A. Hime, *Phys. Rev. D* **73**, 053004 (2006).
  - [8] T. Gaisser, *Cosmic Rays and Particle Physics* (Cambridge University Press, Cambridge, England, 1990).
  - [9] R. Braucher, E. T. Brown, D. L. Bourlès, and F. Colin, *Earth Planet. Sci. Lett.* **211**, 251 (2003).
  - [10] K. J. Kim and P. A. J. Englert, *Earth Planet. Sci. Lett.* **223**, 113 (2004).
  - [11] G. Balco, *Quat. Geochronol.* **39**, 150 (2017).
  - [12] Y.-F. Wang, V. Balic, G. Gratta, A. Fassò, S. Roesler, and A. Ferrari, *Phys. Rev. D* **64**, 013012 (2001).
  - [13] B. Heisinger, D. Lal, A. J. T. Jull, P. Kubik, S. Ivy-Ochs, K. Knie, and E. Nolte, *Earth Planet. Sci. Lett.* **200**, 345 (2002).

- [14] P. Abbon, E. Albrecht, V. Yu Alexakhin, Y. Alexandrov, G. D. Alexeev, M. G. Alekseev, A. Amoroso *et al.*, *Nucl. Instrum. Methods Phys. Res., Sect. A* **577**, 455 (2007).
- [15] C. Ahdida *et al.*, *Front. Phys.* **9**, 788253 (2022).
- [16] S. Abe and T. Sato, *J. Nucl. Sci. Technol.* **53**, 451 (2016).
- [17] L. B. Bezrukov and E. V. Bugaev, *Sov. J. Nucl. Phys.* **33**, 635 (1981).
- [18] T. K. Minorikawa, T. Kitamura, and K. Kobayakawa, *Nuovo. Cimento* **4**, 471 (1981).
- [19] D. E. Groom, N. V. Mokhov, and S. I. Striganov, *At. Data Nucl. Data Tables* **78**, 183 (2001).
- [20] ShinEtsukagakukogyo Ltd. VIOSIL.
- [21] T. Yuguchi *et al.*, *Ganseki. Kobutsu. Kagaku.* **39**, 50 (2010) (in Japanese).
- [22] The Nilaco Corporation NI, 313551.
- [23] Y. Kurebayashi, H. Sakurai, Y. Takahashi, N. Doshita, S. Kikuchi, F. Tokanai, K. Horiuchi *et al.*, *Nucl. Instrum. Methods Phys. Res., Sect. A* **799**, 54 (2015).
- [24] H. Matsuzaki, C. Nakano, H. Yamashita, Y. Maejima, Y. Miyairi, S. Wakasa, and K. Horiuchi, *Nucl. Instrum. Methods Phys. Res., Sect. B* **223–224**, 92 (2004).
- [25] H. Matsuzaki, C. Nakano, Y. S. Tsuchiya, S. Ito, A. Morita, H. Kusuno, Y. Miyake *et al.*, *Nucl. Instrum. Methods Phys. Res., Sect. A* **361**, 63 (2015).
- [26] C. P. Kohl and K. Nishiizumi, *Geochim. Cosmochim. Acta* **56**, 3583 (1992).
- [27] Horiuchi Laboratory, at <http://www.st.hirosaki-u.ac.jp/~kh/>.
- [28] K. Horiuchi, A. Ohta, T. Uchida, H. Matsuzaki, Y. Shibata, and H. Motoyama, *Nucl. Instrum. Methods Phys. Res., Sect. B* **259**, 584 (2007).
- [29] K. Horiuchi and H. Matsuzaki, *Nucl. Instrum. Methods Phys. Res., Sect. B* **361**, 423 (2015).
- [30] R. C. Reedy, K. Nishiizumi, D. Lal, J. R. Arnold, P. A. J. Englert, J. Klein, R. Middleton, A. J. T. Jull, and D. J. Donahue, *Nucl. Instrum. Methods Phys. Res., Sect. B* **92**, 297 (1994).